5. J.S. Hong and M.J. Lancaster, Microstrip filters for RF/microwave applications, Wiley, New York, 2001.
6. C.S. Kim, J.I. Park, A. Dal, et al., A novel 1-D periodic defected ground structure for planar circuits, IEEE Microwave Guided Wave Lett 4 (2000), 131–133.
7. D. Ahn, J.S. Park, C.S. Kim, J. Kim, Y. Qian, and T. Itoh, A design of the low-pass filter using the novel microstrip defected ground structure, IEEE Trans Microwave Theory Tech 1 (2001), 86–93.
8. A. Abdel-Rahman, A.K. Verma, A. Boutejdar, and A.S. Omar, Control of band stop response of hi-low microstrip lowpass filter using slot in ground plane, IEEE Trans Microwave Theory Tech 3 (2004), 1008–1013.
9. A. Abdel-Rahman, A.R. Ali, S. Amari, and A.S. Omar, Compact bandpass filters using defected ground structure (DGS) coupled resonators, IEEE MTT-S Int Dig, Washington, DC (2005), 1479–1482.
10. B. Wu, C.-H. Liang, Q. Li, and P.-Y. Qin, Novel dual-band filter incorporating defected SIR and microstrip SIR, IEEE Microwave Wireless Compon Lett 6 (2008), 392–394.
11. B. Wu, C.-H. Liang, P.-Y. Qin, and Q. Li, Compact dual-band filter using defected stepped impedance resonator, IEEE Microwave Wireless Compon Lett 10 (2008), 674–676.

© 2010 Wiley Periodicals, Inc.

ITERATIVE DESIGN OF MOTH-EYE ANTIREFLECTIVE SURFACES AT MILLIMETER WAVE FREQUENCIES

Mark S. Mirotznik,[1] Brandon Good,[1] Paul Ransom,[2] David Wikner,[3] and Joseph N. Mait[3]
[1] Department of Electrical Engineering and Computer Science, The Catholic University of America, 620 Michigan Ave NE, Washington, DC 20064; Corresponding author: Mirotznik@cua.edu
[2] Carderock Division, Naval Surface Warfare Center, West Bethesda, MD 20817-5700
[3] U.S. Army Research Laboratory, Adelphi, MD 20783

Received 4 June 2009

ABSTRACT: *A method for synthesizing broadband antireflective (AR) surfaces at millimeter wave frequencies is demonstrated. AR surfaces were formed by machining a multilayer subwavelength structures into nonabsorptive dielectrics. This created low-reflected energies (<−25 dB) over large bandwidths and incidence angles. Experimental results are provided demonstrating the validity of the method.* © 2010 Wiley Periodicals, Inc. Microwave Opt Technol Lett 52: 561–568, 2010; Published online in Wiley InterScience (www.interscience.wiley.com). DOI 10.1002/mop.24973

Key words: *diffractive; subwavelength; antireflective; millimeter wave; motheye*

1. INTRODUCTION

Recent advances in passive imaging at millimeter wave frequencies [1–3] have created a need for high-quality optical components, such as lenses, designed specifically for these wavelength bands. For most passive millimeter wave imaging applications, it is of critical importance to collect as much incoming radiation as possible because the signal strengths are commonly many orders of magnitude smaller than intensities encountered at visible or infrared wavelengths. Even at optical wavelengths, however, it is desirable to maximize light collection. To accomplish this condition, antireflective (AR) coatings are often applied to the surface of passive components, such as lenses, to suppress Fresnel reflections and, as a consequence, collect more energy in the desired waveband. The most common method for implementing broadband AR surfaces is to coat the surface with multiple layers of thin films. Various optimization algorithms are used to determine exact values for the number of layers, dielectric constants of the films, and their respective thicknesses such that the coating produces the least amount of reflected energy over the desired spectral band. In general, as the number of layers in the coating increases, the AR behavior improves. Unfortunately, implementing this same approach at millimeter wavelengths can be challenging because finding materials with the desired dielectric constants is difficult. An alternative method, originally developed for designing AR surfaces in visible and infrared applications, uses a multilevel subwavelength grating fabricated directly on the surface of a dielectric [4–7]. This technique was biologically inspired by the subwavelength surface pattern on the cornea of the common moth and many butterflies. In fact, the moth's eye appears completely black because of the AR properties of its subwavelength structure. Consequently, the man-made AR surfaces of this type are often called ''moth-eye'' surfaces. Similar to the conventional thin-film AR coatings, the performance of moth-eye AR surfaces improves as the number of levels increases. This is accomplished, however, at the expense of a more complicated fabrication process. In this article, we present a design algorithm, based on this concept of subwavelength gratings, to construct AR coatings at millimeter wave frequencies. An optimization algorithm, based on a direct pattern search, integrated with a rigorous electromagnetic model (rigorous coupled wave algorithm (RCW)) was used to design AR surfaces at both Ka- and W-band. We validated our design methodology by fabricating an AR surface and characterizing it experimentally.

2. DESIGN METHODOLOGY

2.1. Problem Geometry

Figure 1 depicts the subwavelength grating structures that we investigated to use as an AR surface. The gratings were multilevel (three levels shown in the figure) subwavelength structures with rectangular cross sections. It was assumed that this surface would be machined out of a nonabsorptive dielectric of permittivity, ε_r, and index of refraction, n_r. The period of the gratings along the x and y axes, denoted by Λ_x and Λ_y, respectively, should be smaller than the material wavelength $(i.e.\ \Lambda_x < \frac{\lambda_0}{n_{inc}\sin(\theta)\cos(\phi)},\ \Lambda_y < \frac{\lambda_0}{n_{inc}\sin(\theta)\sin(\phi)})$ to avoid any propagating diffracted orders, other than the zeroth order. Additionally, we assumed that the grating periods, Λ_x and Λ_y, were equal

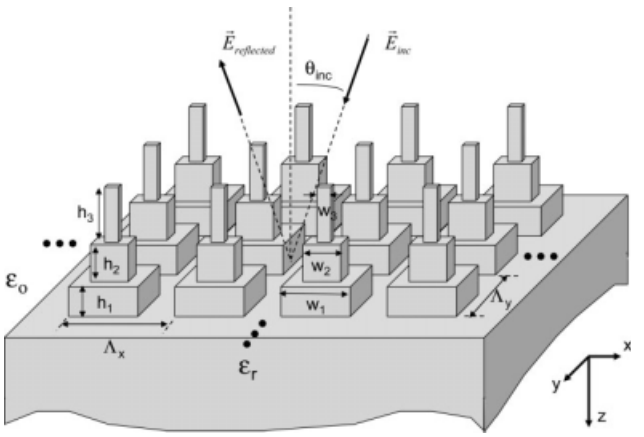

Figure 1 Illustration of the subwavelength geometries used to construct moth-eye-based AR surfaces

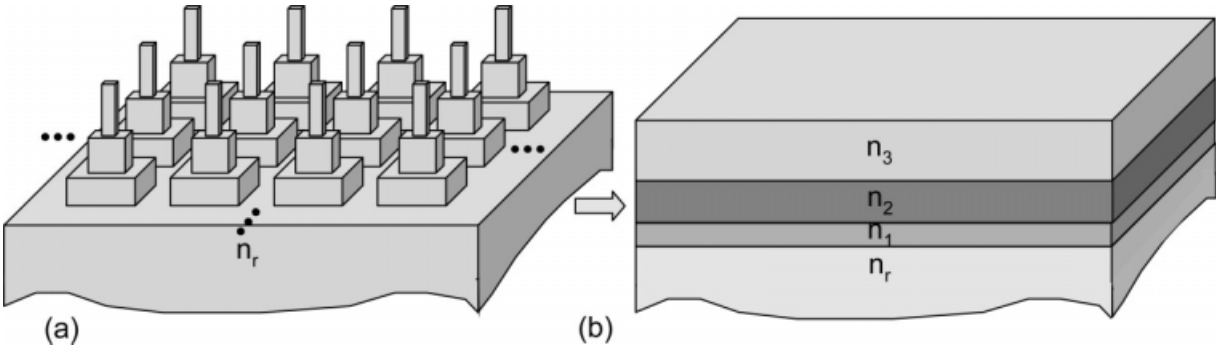

Figure 2 The direct design method assumed that a multileveled subwavelength structure (a) can be approximated by a multilayered dielectric stack (b) with the computed ''effective'' electromagnetic properties of the grating

and will be denoted simply by Λ for the rest of this article. A square cross-sectional grating was motivated by our desire to produce an isotropic AR surface. For other applications, however, it might be desirable to produce anisotropic behavior by assigning different values to Λ_x and Λ_y. The cross-sectional width and height of the nth grating level are denoted by w_n and h_n, respectively. The goal is, thus, to determine the best values for Λ, h_n, and w_n such that the grating surface reflects a minimum amount of energy over the desired frequency band and incident angles. In the examples presented in this article, the incident field is restricted to TE polarized plane waves propagating at an angle θ_{inc} with respect to the z-axis (as illustrated in Fig. 1). However, the algorithm could be applied, without modification, to problems involving plane waves of arbitrary incident angles and polarizations.

2.2. Electromagnetic Modeling

Two approaches are generally reported in the literature for simulating the electromagnetic properties of subwavelength gratings. The first uses effective media theory [8] to provide closed-form approximations for the effective dielectric constants as a function of the grating structure. Although attractive from a computational perspective, the approximate expressions are accurate only for gratings whose period is much smaller than the wavelength of illumination. As the grating period approaches the wavelength, which is referred to as the resonance regime, the assumptions on which these closed-form expressions are based are no longer valid. For our designs, we assumed that grating periods are only slightly smaller than the material wavelength and, thus, could not accurately use the effective media theory.

We used a second approach that uses a rigorous electromagnetic model to determine the relationship between structural form and response. Although computationally more difficult, this approach is capable of generating accurate results for gratings of any period size and shape. Several rigorous electromagnetic models can be used for this calculation. We chose the RCW algorithm originally presented by Moharam and Gaylord [9, 10]. Our specific implementation, based on the method described by Noponen and Turunen [11], was used to calculate the complex transmission and reflection coefficients from multilevel two-dimensional subwavelength gratings. For brevity, the mathematical details of the RCW method are not described here. For a detailed description, the reader can refer to Ref. [11].

2.3. Direct Design Algorithm using Effective Chebyshev Quarter-Wavelength Transformers

In this section, we present a direct method of designing moth-eye AR surfaces by mapping the ''effective'' properties of the subwavelength structure to the dielectric properties of a multilayered dielectric stack. The first step was to use conventional AR coating design algorithms to construct an interference filter (Fig. 2). Although there are large number of good algorithms for designing AR interference filters, we chose to implement the equal ripple antireflective coating algorithm originally described by Collin [12–15]. In Collin's method, each layer of a multilayered dielectric stack is designed to be of quarter-wavelength phase thickness at the center frequency, f_0, of the band of interest (i.e., $\phi(f_0) = 90°$). Under these conditions, the reflectance function, $R(f)$, as a function of frequency, f, for a stack of M layers can be written in the following polynomial form:

$$R(f) = 1 - \frac{1}{c_0\cos^{2M}(\phi(f)) + c_1\cos^{2M-1}(\phi(f)) + \cdots + c_{2M}} \quad (1)$$

where the coefficients, c_i, depend on the refractive indices, n_i, of each layer. By properly selecting the refractive indices, a reflectance function can be derived with desirable AR characteristics. Because of their equal ripple character, the Chebyshev polynomials are a particularly attractive choice. By fitting Eq. (1) to the Chebyshev polynomials Collin's derived equations for the refractive indices gives the total number of layers, M, and desired fractional bandwidth, $\Delta f/f_o$. Although Collin only derived equations for up to four layers, Riblet presented a recursive algorithm that could be used to determine n_i for an arbitrary number of layers [12]. The mathematical details of the Collin–Riblet algorithm are described in numerous references and for the sake of brevity are not presented here.

The next step was to construct a multilayered subwavelength grating in which each layer had the same thickness and ''effective'' refractive indices as the multilayered design found via Collin's method. This is illustrated in Figure 2. To evaluate the effective properties, we first studied a single-subwavelength grating layer as shown in Figure 3. Using RCW theory, the effective index of refraction was determined for this single layer by calculating the zeroth-order reflection and transmission coefficients as a function of the grating's geometry (i.e., Λ, h, and w). Once the zeroth-order reflection coefficients are calculated, the effective index of refraction, denoted by n_{eff}, can be determined by solving the transcendental equation as given in Eq. (2).

$$r_{\text{input}} = n_{\text{eff}}\frac{\left(n_{\text{exit}} + jn_{\text{eff}}\tan\left(\frac{2\pi f}{c}n_{\text{eff}}h\right)\right)}{\left(n_{\text{eff}} + jn_{\text{exit}}\tan\left(\frac{2\pi f}{c}n_{\text{eff}}h\right)\right)} \quad (2)$$

where r_{input} is given by $r_{\text{input}} = n_{\text{incident}}\frac{1-r_o}{1+r_o}$.

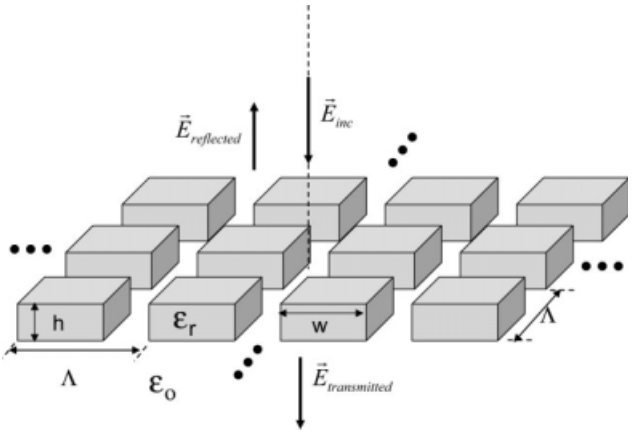

Figure 3 A single binary grating, as shown above, was used to compute the effective material properties of each layer within the multileveled subwavelength structure (shown in Fig. 2a)

Here, n_{exit} and n_{incident} denote the index of refraction of the exit region and incident regions, respectively, and r_0 denotes the zeroth-order reflection coefficient of the grating calculated by the RCW algorithm. These calculations were only conducted at the center wavelength of the frequency band of interest. Figure 4 illustrates a typical effective index variation of the single layer as a function of the grating's fill factor, (w/Λ), and height, h. We then assumed that when single-level gratings are stacked to produce a multilevel structure, the effective properties of each level could be approximated by the effective properties of the single layer. The authors fully acknowledge that in a multilevel grating, the effective properties will depend on the upper- and lower-boundary conditions of each level in addition to being frequency dependent. However, as illustrated latter by examples, did this direct design method provide reasonably good results? Most often, however, the grating designs generated by this direct method provided excellent initial conditions for the iterative optimization algorithm described in the next section.

2.4. Iterative Design Algorithm using Pattern Search Optimization

To refine the solution of the direct design method, we implemented an iterative optimization algorithm as shown in Figure 5. Here, the RCW method is used to calculate the full-wave solution for the reflected energy of any specific grating structure as a function of frequency and angle of incidence. An optimization algorithm is then used to refine the grating geometry such that an objective function is minimized. The objective function we chose to minimize was simply the sum of squared reflection coefficients, r, at a discrete number of frequencies within the band of interest, f_i, and a discrete number of angles of incidence, θ_j, as given in Eq. (3).

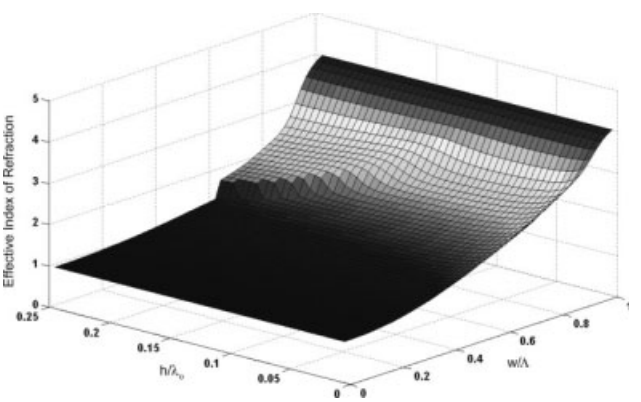

Figure 4 Example illustrating how the effective index of refraction of a binary grating (shown in Fig. 3) varies as a function of the fill factor (w/Λ) and normalized height (h/λ_0) of the grating. The substrate for this example had a index of refraction $n = 4$

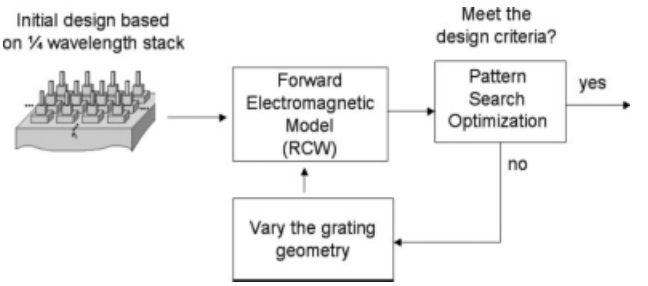

Figure 5 Illustration of the iterative algorithm used to improve the results from the direct design method

$$F = \min\left[\sum_{j=1}^{M}\sum_{i=1}^{N}|r(f_i,\theta_j)|^2\right] \tag{3}$$

A number of iterative optimization algorithms could be used to refine the Chebyshev quarter-wavelength transformer based designs discussed in the above section. These include traditional derivative-based algorithms, genetic algorithms or direct pattern search algorithms. An advantage of both genetic and pattern search algorithms is that they do not require derivatives, and they work well on nondifferentiable, stochastic, and discontinuous objective functions. Both simple genetic algorithms and

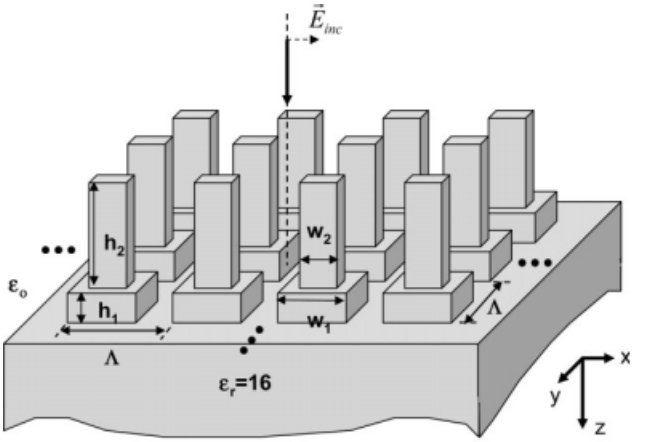

Direct design	Iteratively refined design
w_2=0.66 mm	w_2=0.70 mm
w_1=1.1 mm	w_1=1.10 mm
h_2=1.49	h_2=1.5 mm
h_1=0.77	h_1=0.84 mm
Λ=1.25 mm	Λ=1.25 mm

Figure 6 A two-level subwavelength grating designed as an AR surface in the Ka-band (27–40 GHz) at normal incidence. The substrate was assumed to have a dielectric constant of $\varepsilon_r = 16$. Shown above are the geometric parameters designed using both the direct method and the iterative refinement

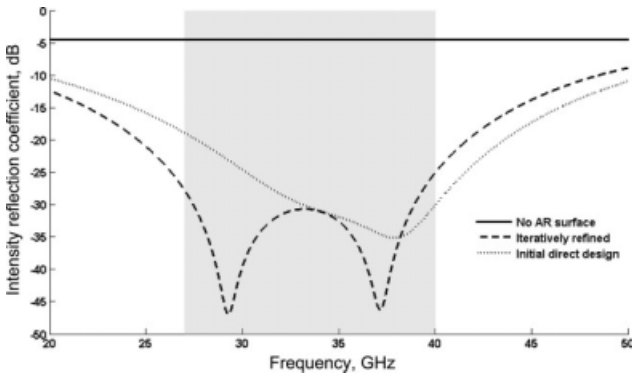

Figure 7 Simulated results, using the RCW method, for the AR moth-eye surface are shown in Figure 6. As a baseline for comparison also presented is the reflected intensity coefficient when no AR surface is added. The dark area represents the frequency band in which the optimization was conducted

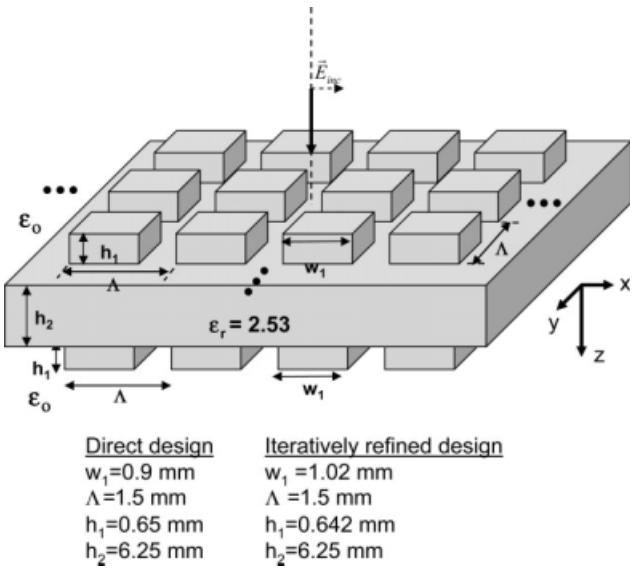

Direct design	Iteratively refined design
w_1=0.9 mm	w_1 =1.02 mm
Λ=1.5 mm	Λ =1.5 mm
h_1=0.65 mm	h_1=0.642 mm
h_2=6.25 mm	h_2=6.25 mm

Figure 8 Moth-eye AR surfaces placed on both sides of a finite thickness dielectric slab of Rexolite^{TM} ($\varepsilon_r = 2.53$). Each surface is a single level (i.e., binary grating) designed as AR in the W-band (90–100 GHz) at normal incidence. Shown above are the geometric parameters designed using both the direct method and the iterative refinement

direct pattern search algorithms were implemented and tested for the application of interest here. Although both methods produced comparable results, the pattern search algorithm was often computationally less expensive. Similar to genetic algorithms, a pattern search can be effective in finding a global minimum because of the nature of its search. However, the authors fully admit that a comprehensive comparison of the methods was not conducted.

Pattern search works by searching, or polling, a set of points called a mesh, which expands or shrinks depending on whether any point within the mesh has a lower objective function value than the current point. The mesh size can be expanded or contracted about the current point by adjusting a scaling parameter. If the algorithm finds a point within the mesh whose objective function is less than the current point then that is called as a successful poll. After a successful poll, the algorithm moves the current point to the new location and then multiplies the current mesh by a scaling factor greater than one (i.e., expands the mesh). If, however, the poll is unsuccessful then the current point is retained and the algorithm multiplies the current mesh by a scaling factor less than one (i.e., contracts the mesh). The search can be stopped after a minimum pattern size is reached, a maximum number of iterations are exceeded, or the minimum distance between the current points at two consecutive iterations is achieved. We used a constrained pattern search algorithm supplied in the Genetic Algorithm and Direct Search toolbox of the commercial software package MATLAB^{TM} by the Mathworks. In the next section, we present several examples of AR surfaces designed using both the direct and iterative design methods.

3. DESIGN EXAMPLES

3.1. Example 1: Ka-Band (27–40 GHz) Normal Incidence

In this first example, an AR surface was designed to reflect a minimum amount of energy within the Ka-band (27–40 GHz) at normal incidence. We assumed that the substrate in which the AR surface would be formed had a dielectric constant of $\varepsilon_r = 16$ and was infinitely thick (i.e., half-space). We also used only a two-level grating as depicted in Figure 6. The grating period, Λ, was fixed at 1.25 mm but the grating heights, (h_1 and h_2),

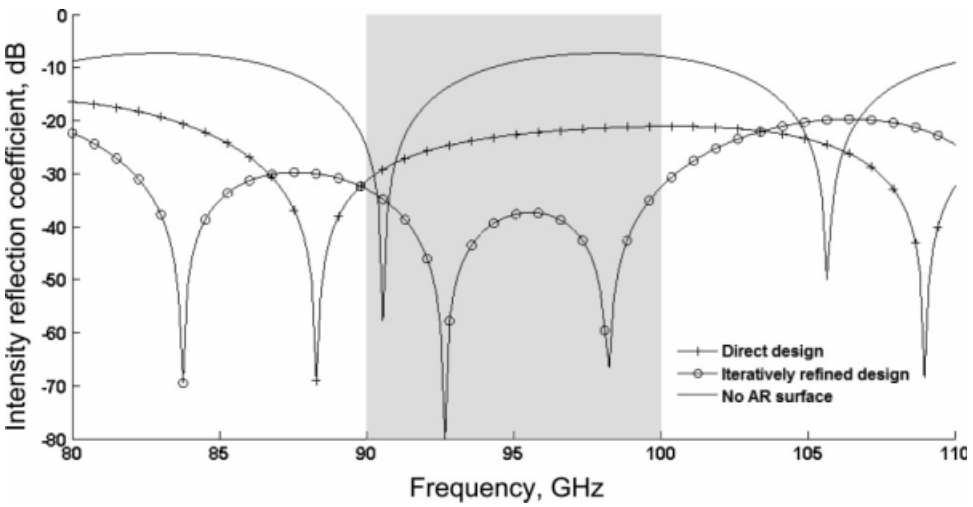

Figure 9 Simulated results, using the RCW method, for the AR moth-eye surface are shown in Figure 8. As a baseline for comparison also presented is the reflected intensity coefficient when no AR surface is added. The dark area represents the frequency band in which the optimization was conducted

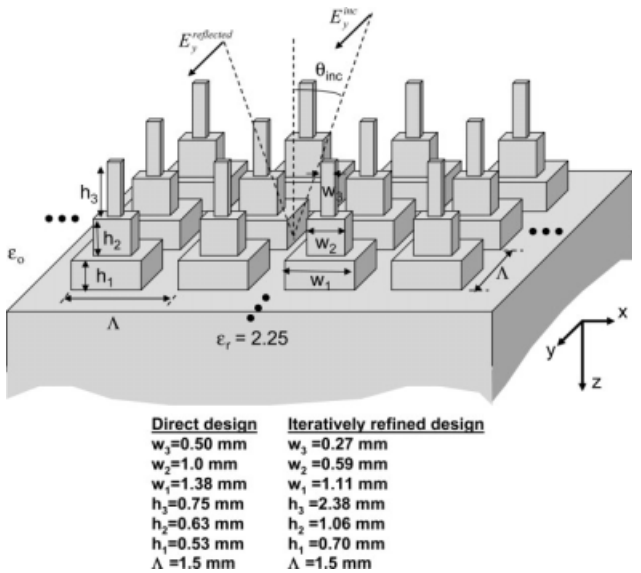

Figure 10 A three-level moth-eye surface designed to be AR in the W-band (90–100 GHz) at incident angles ranging from 0° to 80°. The substrate is Rexolite™ ($\varepsilon_r = 2.53$). Shown above are the geometric parameters designed using both the direct method and the iterative refinement

and widths, (w_1 and w_2), were assumed variable. The geometrical design results using both direct and iterative methods are shown in Figure 6. It is interesting to note that the direct method does a reasonable good job predicting the final iterative design. In fact, the iteratively refined design did not change any of the initial -design parameters by more than 10%. The intensity reflection coefficient, $R = |r|^2$, in dB from these structures is presented in Figure 7. As a baseline for comparison also presented in Figure 7 is the reflection when no AR surface is added. Clearly, both the direct and iterative AR surfaces significantly reduce the reflected energy over the entire frequency band of interest (27–40 GHz). It is also clear that the iterative refinement indeed reduce the reflected energy relative to the initial direct design method. In fact, within the band of interest, R never exceeded −30 dB using the iterative approach. This is an impressive result considering the relatively high-fractional bandwidth (37%) of this example.

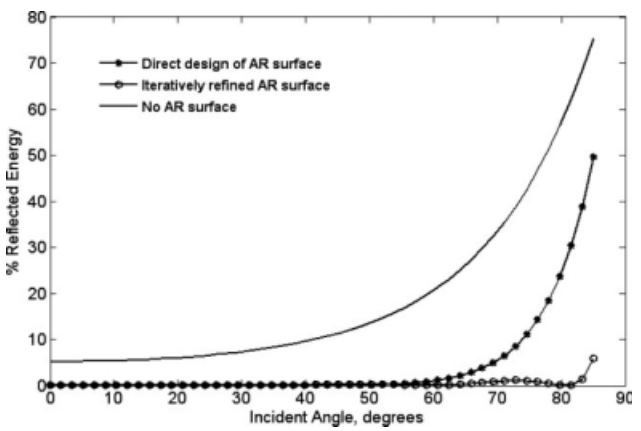

Figure 11 Simulated results for the AR surface are shown in Figure 10. Shown is the percentage of reflected energy as a function of incident angle. For this plot, the frequency was fixed at 95 GHz (i.e., center of the band of interest). As a baseline for comparison also presented is the reflected intensity coefficient when no AR surface is added

TABLE 1 Calculated Reflectance for Example 3, dB for Various Incident Angles

	0°	20°	40°	60°	80°
No-AR surface	−12.8	−12.2	−10.2	−6.6	−2.3
Direct design method	−43.7	−46.0	−40.8	−19.2	−5.7
Iterative design method	−35.3	−43.7	−27.1	−33.9	−31.2

3.2. Example 2: W-Band (90–100 GHz) Normal Incidence

In this second example, a moth-eye-based AR surface was designed for a finite thick planar dielectric slab within the W-band (90–100 GHz). As the previous example, this was also done assuming the normal incidence. The material was assumed to be a finite thick (6.25 mm) slab of Rexolite™ (dielectric constant $\varepsilon_r = 2.53$) with identical moth-eye AR surfaces machined on both the top and bottom surfaces (Fig. 8). The purpose of machining AR gratings on both sides of the substrate was to try to eliminate all Fresnel reflections (i.e., 100% transmission through the substrate). As the fractional bandwidth is relatively small (10/95) only a single level (i.e., binary grating) on each side of the dielectric slab was needed. The grating period, Λ, was fixed at 1.5 mm, and the thickness of the slab, h_2, was fixed at 6.25 mm. The height, h_1, and width, w_1, of the top and bottom subwavelength surface were assumed variable. The geometrical design results using both direct and iterative methods are shown in Figure 8. As in the previous example, the direct method did an excellent job at finding a good initial guess for the iterative algorithm. The intensity reflection coefficient, $R = |r|^2$, in dB is presented in Figure 9. In this case, the result from the iterative algorithm was significantly better than both the no-AR surface case and the direct method. As the previous example within the band of interest R never exceeded −30 dB using the iterative approach.

3.3. Example 3: W-Band (90–100 GHz) at Wide Incident Angles

In this last example, a moth-eye-based AR surface was designed to have a low reflectivity over both frequency and angle of

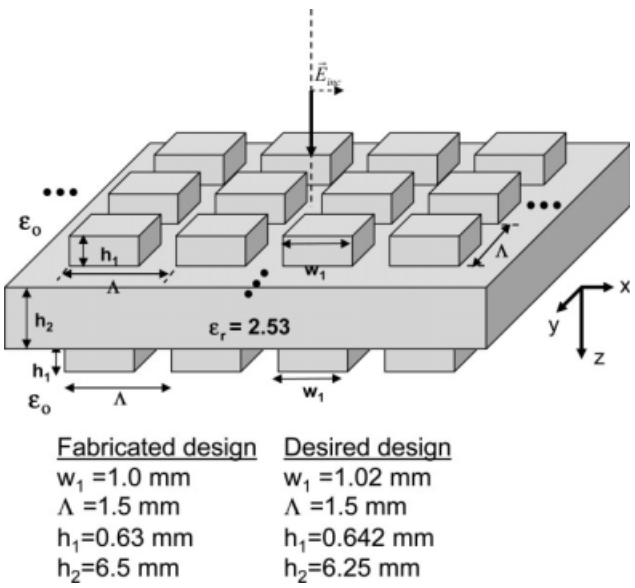

Figure 12 Experimentally measured surface parameters and those calculated via the iterative design algorithm

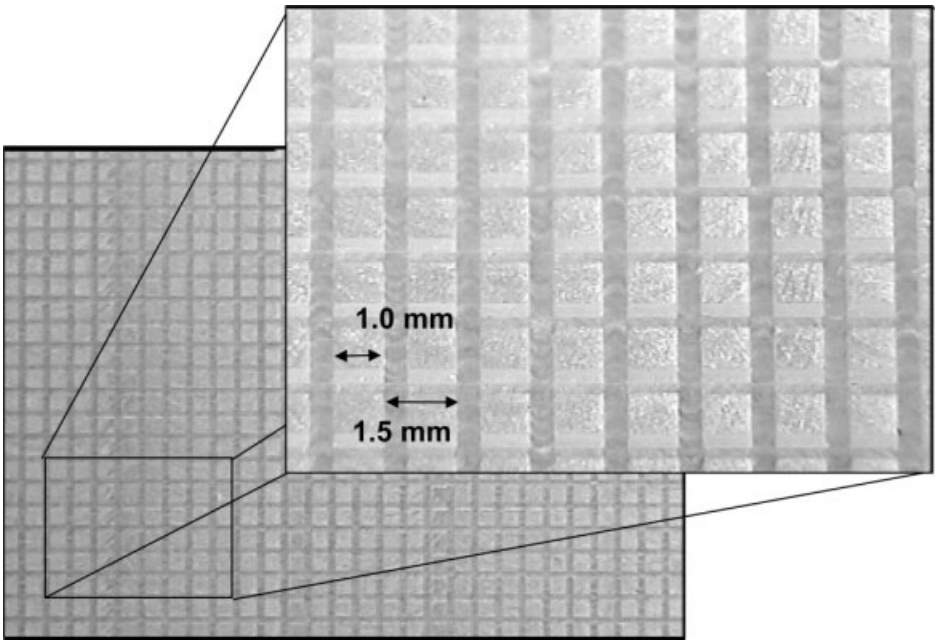

Figure 13 Photograph of the moth-eye AR surface fabricated in Rexolite™

incidence. The incident field, as shown in Figure 10, is assumed to be a TE polarized plane wave in which the angle of incidence, θ_{inc}, as defined in Figure 10, is varied between 0° and 80°. We assumed that the substrate in which the AR surface would be formed is made of Rexolite™(dielectric constant $\varepsilon_r = 2.53$) and was infinitely thick (i.e., half-space). We used a three-level grating for this example. Increasing the number of levels provided the iterative optimization algorithm and the additional degrees of freedom necessary to simultaneously optimize over both frequency and incident angle. The grating period, Λ, was again fixed at 1.5 mm but the grating heights, (h_1, h_2, and h_3), and widths, (w_1, w_2, and w_3), were assumed variable. As in Example #2, the frequency range of interest is the W-band between 90 and 100 GHz. Also, as in the previous examples, the direct method was used to provide an initial structure for the iterative design algorithm. The direct design was conducted only at normal incidence. Considering these restrictions, it is not surprising that the final design parameters (Fig. 10), calculated via the iterative approach, did significantly deviate from the initial design calculated using the direct method. The percent reflected energy as a function of incident angle is shown in Figure 11.

In this Figure, the frequency was fixed at the center of the spectral band (i.e., 95 GHz). Clearly, the iterative optimization algorithm was successful in reducing the amount of reflected energy at all incident angles between 0° and 80°. In fact, the amount of reflected energy never exceeds 1% at any angle. The performance of the direct method, while quite good near normal incidence, quickly deteriorates as the angle of incidence exceeds 60°. It is interesting to note that near normal incidence the direct design method actually outperforms the iteratively optimized design. However, as the incident angle increases, the optimized design begins to perform better, and it is significantly better as the angle exceeds 60°. As there are certainly some physical limits in the AR behavior of a moth-eye surface, the optimization algorithm must be selecting a structure that trades off poorer performance at normal incidence for a better response at the higher incident angles. Table 1 provides more quantitative results of the data presented in Figure 11.

4. EXPERIMENTAL VALIDATION

To validate the performance of our algorithm, we fabricated the design presented in Example #2 and measured the transmissivity and reflectivity within the W-band (75–110 GHz). The moth-eye AR surface, shown in Figure 8, was fabricated from an $18'' \times 18'' \times 0.5''$ plate of Rexolite™ using a three-axis computerized numerical control (CNC) router. The router was instrumented with a 0.5-mm milling bit and provides ~0.01 mm position accuracy. The CNC router was initially used to thin and smooth the surface of the Rexolite™ plate to ~0.3″ (7.75 mm). The

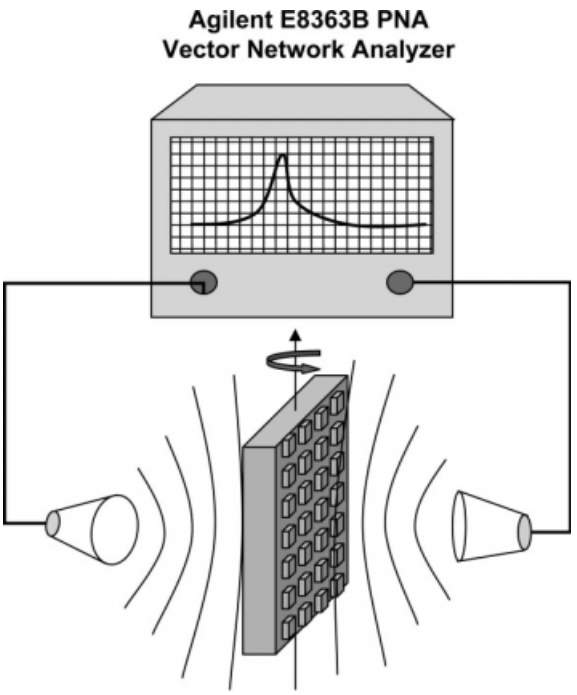

Figure 14 Experimental method used to measure the properties of our samples in both reflection and transmission

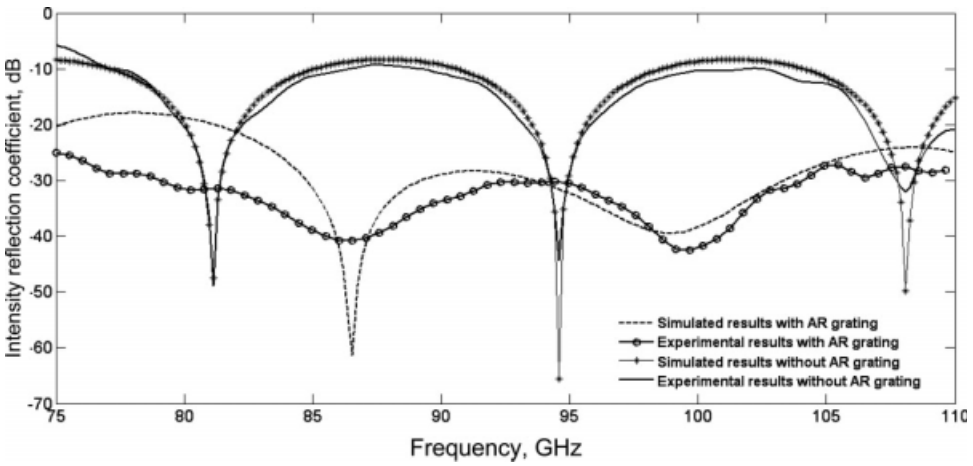

Figure 15 Experimentally measured intensity reflection coefficients, dB, for the samples fabricated with and without the AR grating surface as a function of frequency. Also shown are the simulated results via the rigorous coupled wave method. The incident angle was 0° (normal incidence) for this measurement

router then machined the binary grating, as presented in Figure 8, on both the top and bottom surfaces of the plate. After fabrication, the various feature sizes of the element were measured using an optical microscope. Measurements were taken at a number of locations throughout the sample and then averaged to determine the final values. The experimentally measured surface parameters and those calculated via the iterative design algorithm are given in Figure 12. An image of the fabricated Rexolite^{TM} surface is shown in Figure 13. As a comparison, we also thinned and smoothed a second Rexolite^{TM} plate to a thickness of 7.4 mm. This second plate, however, had no AR surface machined into it and served as a reference.

To measure the properties of the samples in both transmission and reflection, we used the simple arrangement as shown in Figure 14. At the heart of this setup is an Agilent 8363B vector network analyzer with external heads that extends the frequency range to 110 GHz. On the transmit side, a collimating lens was used to form a quasi-plane wave of TE polarization on the surface of the sample. On the receive side, a standard gain horn was used to detect the transmitted energy. The sample was placed on a rotary stage that allowed us to investigate different incident angles. Frequency averaging and time-domain gating were used to remove extraneous reflections.

Experimental results are presented in Figure 15. Here, the measured reflected intensity coefficient at normal incidence is plotted as a function of frequency for both the AR machined sample and the reference sample. Also presented in the figure are the simulated results, using the RCW method, for both samples. For the simulated results, the experimentally measured feature sizes were used. The experimental results confirm the AR behavior of the sample over the entire 75–110 GHz band. In fact, this was a surprisingly good result considering that the optimization was only conducted within the 90–100 GHz frequency range. The maximum intensity reflection coefficient, R, measured in the 90–100 GHz range was -32 dB. As a comparison, the simulation predicts a maximum value of -30 dB. There is also very good agreement between the measured and simulated results for the non-AR machined sample.

5. CONCLUSIONS

In this article, we presented an iterative design algorithm for constructing moth-eye AR surfaces at millimeter wavelengths. Our design method integrated a pattern search optimization algorithm with a rigorous electromagnetic solver to design multilevel subwavelength gratings that create AR behavior over large frequency bandwidths and angles of incidence. Three numerical examples were presented that illustrated the usefulness of this approach in both the Ka- and W-bands. One of the design examples was experimentally fabricated and characterized for validation. We are currently investigating the use of alternative subwavelength shapes (e.g., circular holes) to create AR surfaces that might be easier to fabricate.

REFERENCES

1. L. Yujiri, M. Shoucri, and P. Moffa, Passive millimeter wave imaging, IEEE Microwave Mag 4 (2003), 39–50.
2. R. Appleby and R.N. Anderton, Millimeter-wave and submillimeter-wave imaging for security and surveillance, Proc IEEE 95 (2007), 1683–1690.
3. D.A. Wikner and G. Samples, Polarimetric passive millimeter-wave sensing, in passive millimeter-wave imaging technology, SPIE Proc 4373 (2001), 86–93.
4. J. Santos and L. Bernado, Antireflective structures with use of multilevel subwavelength zero-order gratings, Appl Opt 36 (1997), 8935–8938.
5. R. Brauer and O. Bryngdahl, Design of antireflective gratings with approximate and rigorous methods, Appl Opt 33 (1994), 7875–7882.
6. M. Shokooh-Saremi and M. Mirsalehi, Comparison of antireflective surfaces based on two-dimensional binary gratings and thin-film coatings, Appl Opt 44 (2005), 3877–3884.
7. D.H. Raguin and G.M. Morris, Antireflection structured surfaces for the infrared spectral region, Appl Opt 32 (1993), 1154.
8. P. Lalanne and J. Hugonin, High-order effective-medium theory of subwavelength gratings in classical mounting: application to volume holograms, J Opt Soc Am A 15 (1998), 1843–1851.
9. M.G. Moharam and T.K. Gaylord, Rigorous coupled-wave analysis of planar-grating diffraction, J Opt Soc Am A 71 (1981), 811–818.
10. M.G. Moharam, E.B. Grann, D.A. Pommet, and T.K. Gaylord, Formulation for stable and efficient implementation of the rigorous coupled wave analysis of binary gratings, J Opt Soc Am A 12 (1995), 1068–1076.
11. E. Noponen and J. Turunen, Eigenmode method for electromagnetic synthesis of diffractive element with three-dimensional profiles, J Opt Soc Am A 11 (1994), 2494–2502.
12. R.E. Collin, Foundations of microwave engineering, McGraw-Hill, New York, 1966.

13. R.E. Collin, Theory and design of wide-band multisection quarter-wave transformers, Proc IRE 43 (1955), 179–185.
14. L. Young, Synthesis of multiple antireflective films over a prescribed frequency band, J Opt Soc Am 51 (1961), 967–974.
15. H.J. Riblet, General synthesis of quarter-wave impedance transformers, IRE Trans Microwave Theory Tech MTT-5 (1957), 36–43.

© 2010 Wiley Periodicals, Inc.

A COMPACT ULTRA-WIDE STOPBAND, LOW INSERTION LOSS, AND SHARP CUTOFF LOW-PASS FILTER

Shu-Hong Fu,[1,2] Chuang-Ming Tong,[1,2] Xi-Min Li,[1,2] and Kai Shen[1]
[1] Radar Engineering Department, Missile Institute of Air Force Engineering University, Sanyuan, Shaanxi 713800, China; Corresponding author: fushuhong1982@163.com
[2] State Key Laboratory of Millimeter Wave, Nanjing 210096, China

Received 6 June 2009

ABSTRACT: *A novel compact microstrip low-pass filter (LPF) with ultra-wide stopband, low insertion loss, and sharp cutoff is introduced in this letter. The LPF is composed of a stepped-impedance hairpin resonator, a square split-ring resonator, defected ground structure (DGS), and a pair of coupled DGSs with compensated microstrip lines. Measured results show that the 10-dB stopband is up to 19.62 GHz, passband loss is below 0.5 dB, and the selectivity of the filter is more than 180 dB/GHz, but its occupied area is only 20 × 35 mm^2. It can be widely used for higher harmonics suppression for wideband microwave applications.* © 2010 Wiley Periodicals, Inc. Microwave Opt Technol Lett 52: 568–570, 2010; Published online in Wiley InterScience (www.interscience.wiley.com). DOI 10.1002/mop.24976

Key words: *low-pass filter; stepped-impedance hairpin resonator (SIHR); square split-ring resonator defected ground structure (SSRR DGS); coupled DGSs*

1. INTRODUCTION

Compact and high-performance low-pass filter is highly demanded in many communication systems to suppress harmonics and spurious signals. The conventional stepped-impedance and stubs low-pass filters (LPFs) only provide Butterworth and Chebyshev characteristics with a gradual cutoff frequency response [1]. To obtain a sharp cutoff, these structures require more sections. Unfortunately, increasing the number of sections also increases the size of the filter and insertion loss. Recently, some periodic structures such as photonic-bandgap and defected ground structure (DGS) are applied to design LPFs [2, 3]. However, a similar performance as those of the conventional ones was found. To reduce the filter area and improve the cutoff characteristics, some special DGS cells combined with stepped-impedance hairpin resonator (SIHR) or stubs were adopted, which were typically represented by split-ring resonator DGS and asymmetric DGS [4–7], but their application areas are also limited because of their insufficient suppression in high-frequency range.

In this letter, a compact microstrip LPF with ultra-wide stopband, low insertion loss, and sharp cutoff is presented. The original LPF is based on the SIHR with an interdigital gap. To produce an ultra-wide stopband and sharp cutoff with a compact size, additional attenuation poles are properly allocated and realized by adding square split-ring resonator DGS (SSRR DGS) and coupled DGSs with compensated microstrip lines into the original LPF structure. Moreover, the designed filter exhibits low insertion loss. The proposed LPF is compact and easy to fabricate. Finally, the validity of this design technique is verified by measurements.

2. LOW-PASS FILTER DESIGN

The LPF is proposed, and its layout is shown in Figure 1. The filter consists of a SIHR, a SSRR DGS cell, and a pair of coupled DGSs with compensated microstrip lines. The LPF prototype is based on the SIHR [8]. The SSRR DGS is added into SIHR to improve the cutoff characteristics and lower the insertion loss of filter [7], whereas the coupled DGSs with compensated microstrip lines are designed to make additional attenuation poles and produce an ultra-wide stopband, which can be used to suppression higher harmonics [9, 10].

In Figure 1, the SIHR is described by a stepped-impedance transmission line and coupled lines. The equivalent capacitance of the coupled lines is determined by the interdigital gap g. A pair of coupled DGSs with compensated microstrip lines is

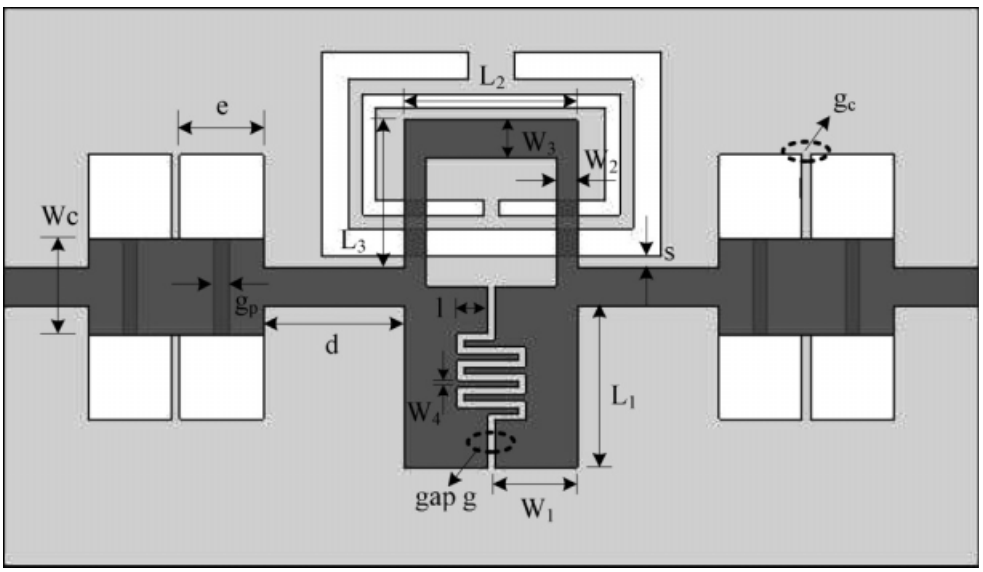

Figure 1 Layout of the proposed LPF